ACADEMIC PRESS

Available online at www.sciencedirect.com
SCIENCE @ DIRECT®

NeuroImage

NeuroImage 18 (2003) 865–879

www.elsevier.com/locate/ynimg

Factors affecting the accuracy of near-infrared spectroscopy concentration calculations for focal changes in oxygenation parameters

Gary Strangman,[a,b,*] Maria Angela Franceschini,[b,c] and David A. Boas[b]

[a] Neural Systems Group, Massachusetts General Hospital, Harvard Medical School, Charlestown, MA 02129, USA
[b] Athinoula A. Martinos Center, Massachusetts General Hospital, Harvard Medical School, Charlestown, MA 02129, USA
[c] Bioengineering Center, Department of Electrical Engineering and Computer Science, Tufts University, 4 Colby Street, Medford, MA 02155-6013, USA

Received 28 January 2002; revised 25 October 2002; accepted 21 November 2002

Abstract

Near-infrared spectroscopy (NIRS) can be used to noninvasively measure changes in the concentrations of oxy- and deoxyhemoglobin in tissue. We have previously shown that while global changes can be reliably measured, focal changes can produce erroneous estimates of concentration changes (NeuroImage 13 (2001), 76). Here, we describe four separate sources for systematic error in the calculation of focal hemoglobin changes from NIRS data and use experimental methods and Monte Carlo simulations to examine the importance and mitigation methods of each. The sources of error are: (1) the absolute magnitudes and relative differences in pathlength factors as a function of wavelength, (2) the location and spatial extent of the absorption change with respect to the optical probe, (3) possible differences in the spatial distribution of hemoglobin species, and (4) the potential for simultaneous monitoring of multiple regions of activation. We found wavelength selection and optode placement to be important variables in minimizing such errors, and our findings indicate that appropriate experimental procedures could reduce each of these errors to a small fraction ($<10\%$) of the observed concentration changes.

Introduction

Diffuse optical methods—whereby light is transmitted through a highly scattering medium for the purpose of making a measurement of that medium—have been in use for over two decades to monitor important hemodynamic variables in tissue. These measurements are made possible by an "optical window" in tissue that spans the near-infrared region (approximately 650–950 nm) of the electromagnetic spectrum. In this region, oxyhemoglobin (HbO_2) and deoxyhemoglobin (HbR) are the dominant absorbers, and their concentrations are sufficiently low (<100 μM) to allow light to pass through several centimeters of tissue and still be detected (Gratton et al., 1994; cf. Jobsis, 1977). The promise of diffuse optical methods lies in their potential to provide absolute quantitation of hemodynamic variables, including [HbO_2] and [HbR] (and the sum of these components, total hemoglobin, [HbT]), as well as potentially cytochrome oxidase concentrations (Cope et al., 1991; Elwell et al., 1994; Hock et al., 1995; Hueber et al., 2001; Kohl et al., 1998; Kurth et al., 1993; Quaresima et al., 1998; Tamura et al., 1997).

Near-infrared spectroscopy (NIRS) is an increasingly popular, noninvasive method for monitoring these hemodynamic variables. NIRS has been used in a variety of applications including fetal monitoring (e.g., Aldrich et al., 1994; Parilla et al., 1997; Peebles et al., 1992), cardiac surgery (for a review, see Nollert et al., 2000), muscle monitoring (e.g., Chance, 1991; Duncan et al., 1995; Franceschini et al., 1997; Nioka et al., 1998), and a wide variety of studies on brain function (cf. Chance, 1991; Villringer and Chance, 1997). To accurately quantify [HbR] and [HbO_2], the relative contributions of these two absorbers must be separated from the raw optical signals. To do so, measurements at two or more wavelengths are simultaneously acquired, and a model is applied to convert the wavelength data to chromophore concentrations.

The standard model used to perform this conversion is

---

* Corresponding author. Neural Systems Group, 149 13th Street, Room 9103, Charlestown, MA 02129. Fax: +1-617-726-4078.
E-mail address: strang@nmr.mgh.harvard.edu (G. Strangman).

1053-8119/03/$ – see front matter © 2003 Elsevier Science (USA). All rights reserved.
doi:10.1016/S1053-8119(03)00021-1

based on the modified Beer–Lambert law (MBLL; Delpy et al., 1988). This model is highly dependent on knowledge about the spatial location and extent of any change in [HbR] and/or [HbO_2] within the light-sampling region. For some measures—for example, in muscle—the simple assumption that concentration changes are global within the tissue may hold to a reasonable degree. For measurements in other settings, however, such as functional brain activation, this assumption is clearly violated. In an adult human, the scalp and skull range from approximately 1 to 2 cm thick, depending on the subject and the region on the head. Consistent negative findings from whole-head functional MRI scanning indicate that these layers often exhibit little or no change in hemodynamic variables during a wide variety of tasks. Even within the brain, while gray matter exhibits substantial changes under functional loading, the activated regions are commonly less than 1 cm across—a spatial scale that is focal relative to the sampling region with source-detector separations ranging from 2 to 5 cm. Hence, the activated region in this situation will constitute only a small fraction—less than 10%—of the entire sampling region.

In a previous report (Boas et al., 2001), we demonstrated that when deriving Δ[HbR] and Δ[HbO_2] from NIRS data using the MBLL with a global-change assumption, serious errors can arise when such a focal change is actually present. These errors are systematic and are a function of the positioning of the source and detector relative to the focal change in chromophores. We argued that, as a consequence of the changes being local *and* unknown in position relative to the source and detector, [HbR] and [HbO_2] cannot, in general, be quantified in an absolute sense by NIRS. We also argued that imaging (as opposed to point measurements) is one solution to this quantification problem.

In this article, we elaborate on our previous findings by pointing out other potential sources of systematic error in computing concentrations as well as by providing guidelines for reducing such errors in the absence of imaging. To do so will first require two definitions. The differential pathlength factor (DPF) is the scaling factor that relates source-detector separations to the average path length light travels between the source and detector. The DPF is a function of wavelength and can be measured by time-domain and frequency-domain systems. Tabulated values exist for various tissues (Duncan et al., 1995; Essenpreis et al., 1993), although the values do vary across subjects and over time even for a given subject and tissue (Duncan et al., 1996). The notion of a DPF implies the assumption that the chromophore change is global to the sampling region. In contrast, the term partial pathlength factor (PPF) will refer to a similar scaling factor, but one that instead assumes a focal change. A PPF therefore represents a proportionality factor converting the source-detector separation into the average path length that light travels through a *focal* region of chromophore change (Hiraoka et al., 1993; Steinbrink et al., 2001).

We argue that there are four potential sources of error to be considered when analyzing raw NIRS data using the MBLL. They are as follows: (1) the absolute magnitudes and relative differences in pathlength factors as a function of wavelength, (2) the location and spatial extent of the absorption change with respect to the optical probe and the resulting PPFs, (3) possible differences in the spatial distribution of hemoglobin species and the resulting species-specific PPFs (e.g., PPF_{HbR} and so on), and (4) the potential for simultaneous monitoring of multiple regions of activation. The optical researcher's goal is to minimize the effect of any such errors. We demonstrate both empirically (in particular see Fig. 3) and with simulations that wavelength selection (point 1, above) is an important parameter—suggesting that proper wavelength selection can help to minimize PPF-related systematic errors. We also show experimental evidence that simply optimizing optical signals (i.e., optimizing optode position relative to the focal change) can also minimize PPF-related systematic errors (point 2). We quantify the effects related to all four points via several Monte Carlo simulations on a realistic head model that examine the sensitivity of optical analysis to the effects of spatial location, differential species distribution, and multiple activation sites. In summary, we found that careful experimental choices should limit these errors to a small fraction (<10%) of the observed concentration changes.

Theory of the modified Beer–Lambert law

The modified Beer–Lambert law is typically used to describe the change in light attenuation in scattering media because of absorption changes (which in turn result from changes in chromophore concentrations). When the change in absorption is global throughout the medium, then the MBLL is written as

$$\begin{aligned}\Delta \mathrm{OD}(\lambda) = \Delta \mu_a(\lambda) L \ell_{\mathrm{DPF}}(\lambda) &= [\varepsilon_{\mathrm{HbO2}}(\lambda)\Delta[\mathrm{HbO}_2] \\ &\quad + \varepsilon_{\mathrm{HbR}}(\lambda)\Delta[\mathrm{HbR}]] L \ell_{\mathrm{DPF}}(\lambda), \qquad (1)\end{aligned}$$

where $\Delta OD(\lambda)$ is the change in optical density measured at a given wavelength, $\Delta\mu_a(\lambda)$ is the corresponding change in tissue absorption, L is the separation between the source and detector, and $\ell_{DPF}(\lambda)$ is the differential pathlength factor (unitless), which accounts for the increased distance that light travels from the source to the detector because of scattering and absorption effects (in the presence of no scattering $\ell_{DPF}(\lambda) = 1$). As shown in the second line, the change in absorption is related to changes in the chromophore concentrations of oxyhemoglobin ($\Delta[HbO_2]$) and deoxyhemoglobin (Δ[HbR]) by the extinction coefficients $\varepsilon_{HbO2}(\lambda)$ and $\varepsilon_{HbR}(\lambda)$, which are wavelength dependent. From measurements of $\Delta OD(\lambda)$ at two wavelengths, the concentration changes are given by

$$\Delta[\mathrm{HbR}] = \frac{\varepsilon_{\mathrm{HbO2}}(\lambda_2)\Delta\mu_a(\lambda_1) - \varepsilon_{\mathrm{HbO2}}(\lambda_1)\Delta\mu_a(\lambda_2)}{\varepsilon_{\mathrm{HbR}}(\lambda_1)\varepsilon_{\mathrm{HbO2}}(\lambda_2) - \varepsilon_{\mathrm{HbO2}}(\lambda_1)\varepsilon_{\mathrm{HbR}}(\lambda_2)}$$

$$\Delta[\mathrm{HbO_2}] = \frac{\varepsilon_{\mathrm{HbR}}(\lambda_1)\Delta\mu_a(\lambda_2) - \varepsilon_{\mathrm{HbR}}(\lambda_2)\Delta\mu_a(\lambda_1)}{\varepsilon_{\mathrm{HbR}}(\lambda_1)\varepsilon_{\mathrm{HbO2}}(\lambda_2) - \varepsilon_{\mathrm{HbO2}}(\lambda_1)\varepsilon_{\mathrm{HbR}}(\lambda_2)}. \tag{2}$$

When the change in absorption is not global, the modified Beer–Lambert law can be rewritten as

$$\begin{aligned}\Delta\mathrm{OD}(\lambda) &= L\sum_{i=1}^{N}\Delta\mu_{a,i}(\lambda)\ell_{\mathrm{PPF},i}(\lambda)\\ &= L\sum_{i=1}^{N}[\varepsilon_{\mathrm{HbO2}}(\lambda)\Delta[\mathrm{HbO_2}]\\ &\quad + \varepsilon_{\mathrm{HbR}}(\lambda)\Delta[\mathrm{HbR}]]\ell_{\mathrm{PPF},i}(\lambda),\end{aligned} \tag{3}$$

where $\ell_{\mathrm{PPF},i}(\lambda)$ is the partial pathlength factor (unitless) through a region of uniform absorption change. A sum is performed over N regions of uniform absorption change. This notation has been used by Steinbrink et al. (2001) to study the sensitivity to tissue layers at different depths.

Cross-talk between oxy- and deoxyhemoglobin

In the case of brain activation, the measured change in optical density is best analyzed with a PPF, because of the focal nature of the brain activation. Unfortunately, accurate estimation of the PPF is not feasible because it requires knowledge of the position and spatial extent of the local absorption change, as well as the optical properties of the surrounding tissue. For this reason, the DPF is used in most analyses (e.g., Franceschini et al., 2000; Tamura et al., 1997).

Systematic errors in the choice of the pathlength factor result in systematic errors in the estimated concentration changes, which can lead to cross-talk between species in the estimated concentration changes (e.g., Boas et al., 2001). For example, if we measure the change in optical density due to a local absorption change ($\Delta\mathrm{OD}_{\mathrm{real}}$ as given by Eq. (3)) and compare that to an estimate of the absorption change using the differential pathlength factor ($\Delta\mathrm{OD}_{\mathrm{estim}}$ as given by Eq. (1)) we find that we underestimate the absorption change. That is, we assume that $\Delta\mathrm{OD}_{\mathrm{estim}} = \Delta\mathrm{OD}_{\mathrm{real}}$, and as a result we obtain the following expression for our underestimation:

$$\Delta\mu_{a,\mathrm{estim}}(\lambda) = \frac{\ell_{\mathrm{PPF}}(\lambda)}{\ell_{\mathrm{DPF}}(\lambda)}\Delta\mu_{a,\mathrm{real}}(\lambda). \tag{4}$$

The estimated absorption change ($\Delta\mu_{a,\mathrm{estim}}$) will always be smaller than the real absorption change because the PPF is always smaller than the DPF. Thus, the estimated concentration changes will always be smaller than the real concentration changes. This is more generally known as a partial volume effect.

The potential for cross-talk between the estimated oxy- and deoxyhemoglobin concentrations is found by first relating the estimated concentration changes to the estimated absorption changes (Eq. (2)), substituting the real absorption change for the estimated absorption change using Eq. (4), and then substituting the real concentration changes for the real absorption changes (as done in Eq. (1)). A few lines of algebra indicates that

$$\Delta[\mathrm{X}]_{\mathrm{estim}} = P\Delta[\mathrm{X}]_{\mathrm{real}} + C\Delta[\mathrm{O}]_{\mathrm{real}}, \tag{5}$$

where [X] represents either [HbO$_2$] or [HbR] and correspondingly [O] represents the *other* species [HbR] or [HbO$_2$], respectively. P indicates the partial volume reduction in the estimated species concentration and C indicates the cross-talk from the other species, as given by

$$\begin{aligned}P &= \left[\frac{-k(\lambda_1)\varepsilon_{\mathrm{X}}(\lambda_1)\varepsilon_{\mathrm{O}}(\lambda_2) + k(\lambda_2)\varepsilon_{\mathrm{O}}(\lambda_1)\varepsilon_{\mathrm{X}}(\lambda_2)}{[\varepsilon_{\mathrm{O}}(\lambda_1)\varepsilon_{\mathrm{X}}(\lambda_2) - \varepsilon_{\mathrm{X}}(\lambda_1)\varepsilon_{\mathrm{O}}(\lambda_2)]}\right]\\ &= Ak(\lambda_1) + Bk(\lambda_2)\\ C &= \frac{-\varepsilon_{\mathrm{O}}(\lambda_1)\varepsilon_{\mathrm{O}}(\lambda_2)}{\varepsilon_{\mathrm{O}}(\lambda_1)\varepsilon_{\mathrm{X}}(\lambda_2) - \varepsilon_{\mathrm{X}}(\lambda_1)\varepsilon_{\mathrm{O}}(\lambda_2)}[k(\lambda_1) - k(\lambda_2)]\\ &= D[k(\lambda_1) - k(\lambda_2)],\end{aligned} \tag{6}$$

where $k(\lambda) = \ell_{\mathrm{PPF}}(\lambda)/\ell_{\mathrm{DPF}}(\lambda)$ (or more generally written as $k(\lambda) = \ell_{\mathrm{real}}(\lambda)/\ell_{\mathrm{estim}}(\lambda)$) indicates the error in the pathlength factor (or the partial volume effect) at each wavelength. Note that when the error at each wavelength is the same, the cross-talk $C = 0$. The parameters A, B, and D are simply a function of wavelength and are plotted in Fig. 4c for HbO$_2$ (left) and HbR (right).

Cross-talk from species-dependent pathlength factors

Now consider the possibility that a localized brain activation results in oxy- and deoxyhemoglobin changes with different spatial locations and/or spatial extents. For example, the [HbR] change appears predominantly in the venous compartment while the [HbO$_2$] change appears in all vascular compartments. Moreover, there are experimental indications that the region of HbO$_2$ change during functional activation is spatially larger than that of HbR (e.g., Duong et al., 2000; Franceschini et al., 2000; Hu et al., 1997). In this case, we need different PPFs for each species. Considering only one region of activation, we then have

$$\begin{aligned}\Delta\mathrm{OD}_{\mathrm{real}}(\lambda) &= [\varepsilon_{\mathrm{HbO2}}(\lambda)\Delta[\mathrm{HbO_2}]\ell_{\mathrm{PPF,\,HbO2}}(\lambda)\\ &\quad + \varepsilon_{\mathrm{HbR}}(\lambda)\Delta[\mathrm{HbR}]\ell_{\mathrm{PPF,\,HbR}}(\lambda)]L,\ \text{and}\end{aligned} \tag{7a}$$

$$\begin{aligned}\Delta\mu_{a,\mathrm{estim}}(\lambda) &= \frac{\ell_{\mathrm{PPF,\,HbO2}}(\lambda)}{\ell_{\mathrm{DPF}}(\lambda)}\Delta\mu_{a,\mathrm{HbO2}}(\lambda)\\ &\quad + \frac{\ell_{\mathrm{PPF,\,HbR}}(\lambda)}{\ell_{\mathrm{DPF}}(\lambda)}\Delta\mu_{a,\mathrm{HbR}}(\lambda)\end{aligned} \tag{7b}$$

By substituting Eq. (7b) into Eq. (2), errors in our estimate of the pathlength factor will still produce errors in the estimated concentration change according to Eq. (5) but with

$$P = Ak_X(\lambda_1) + Bk_X(\lambda_2)$$
$$C = D[k_O(\lambda_1) - k_O(\lambda_2)] \quad (8)$$

A, B, and *D* have the same form as in Eq. (6). The error in the pathlength factor is now species dependent where X indicates the same species and O indicates the other species (see Eq. (5)), such that $k_X(\lambda) = \ell_{PPF,X}(\lambda)/\ell_{DPF,X}(\lambda)$ and $k_O(\lambda) = \ell_{PPF,O}(\lambda)/\ell_{DPF,O}(\lambda)$. More generally, the subscripts PPF and DPF could be replaced with real and estimated, respectively. Once again note that when the PPF-related error at each wavelength is the same, the cross-talk $C = 0$.

Cross-talk between two different activation regions

Finally, consider the possibility of a brain stimulus resulting in two separate activation foci (labeled α and β). In this case,

$$\begin{aligned}\Delta OD_{real}(\lambda) = {} & [\varepsilon_{HbO2}(\lambda)\Delta[HbO_2]_\alpha \\ & + \varepsilon_{HbR}(\lambda)\Delta[HbR]_\alpha]\ell_{PPF,\alpha}(\lambda)L \\ & + [\varepsilon_{HbO2}(\lambda)\Delta[HbO_2]_\beta \\ & + \varepsilon_{HbR}(\lambda)\Delta[HbR]_\beta]\ell_{PPF,\beta}(\lambda)L. \quad (9)\end{aligned}$$

Errors in the estimate of the pathlength factors will then produce errors in the estimate of the concentration change at one focus of the form

$$\begin{aligned}\Delta[X]_{estim,\alpha} = {} & P_\alpha\Delta[X]_{real,\alpha} + C_\alpha\Delta[O]_{real,\alpha} \\ & + P_\beta\Delta[X]_{real,\beta} + C_\beta\Delta[O]_{real,\beta}, \quad (10)\end{aligned}$$

where P_α and C_α are given by Eq. (6) but with $k(\lambda) = k_\alpha(\lambda) = \ell_{PPF,\alpha}(\lambda)/\ell_{DPF,\alpha}(\lambda)$. P_β and C_β are also given by Eq. (6) but with $k(\lambda) = k_\beta(\lambda) = \ell_{PPF,\beta}(\lambda)/\ell_{DPF,\beta}(\lambda)$.

Materials and methods

To examine the quantitative importance of these theoretical derivations, we performed two types of studies: (1) NIRS experiments using a simple motor task designed to illustrate the theoretical points and (2) several Monte Carlo simulations on a tissue-segmented model based on an individual MRI scan to help quantify the effect of the four described sources of errors in a general NIRS-type experiment.

NIRS

Instrumentation and setup

A simple, unimanual motor task was used to examine the cross-talk in calculating [HbR] and [HbO$_2$] for different wavelength pairs. The study was approved by the Institutional Review Board of Tufts University, where the human experiments were performed, and all subjects (three men, ages 27, 29, and 54 years) gave their written informed consent. An ISS frequency-domain tissue spectrometer (Model 96208, ISS, Inc., Champaign, IL) was used for the NIRS recording. Two source fibers were attached to an elastic cap and positioned 1.6 and 2.8 cm posterior to position C3 in the EEG 10–20 system, because it has been shown that C3 lies approximately over the hand area of the left primary motor cortex (Steinmetz et al., 1989). Each source was composed of eight laser diodes emitting at 636, 675, 691, 752, 780, 788, 830, and 840 nm, respectively, which were fed into a 2-mm bifurcated fiber. One detector fiber, 3 mm in diameter, was also attached to the elastic cap, positioned 1.8 cm anterior to C3 (on the line formed by C3 and the sources). We report experimentally calculated [HbR] and [HbO$_2$] results for just 691, 752, and 780 nm paired with 830 nm because of (1) low signal amplitudes from 636 and 675 nm, (2) signals from 788 and 840 nm were virtually identical to those collected at 780 and 830, respectively, and (3) to improve figure clarity.

DPF measurement

Prior to commencing each NIRS recording, DPFs were measured by quantifying the tissue absorption coefficient and the reduced scattering coefficient using the frequency-domain multidistance method (for details, see Fantini et al., 1994). This method allows determination of the DPF at multiple wavelengths in the absence of a measure of absolute phase, as is the case for the ISS instrument. The multidistance scheme was implemented by considering the data collected by the two source fibers located at two different distances (3.6 and 4.8 cm) from the detector fiber. Details on this hybrid frequency-domain (to measure the DPF) and continuous-wave (modified Beer–Lambert law) approach have been described elsewhere (Fantini et al., 1999). To determine the DPF at the eight wavelengths we averaged 200 points during 32 s of baseline (the 16 lasers were turned on one at a time for 10 ms each, i.e., acquisition time per data point 160 ms). Once the DPF was measured, we turned off the source at the larger distance from the detector and acquired NIRS data from each of the eight wavelengths every 80 ms.

Protocol

During the experiment, the subject was asked to rest quietly in a supine position. When the experimental run began, the subject alternated between rest for 17 s and 15 s of four-finger flexion/extension with the four fingers of the right hand. The subject performed 10 such 15-s blocks of the motor task, interleaved with 11 blocks of rest, for a total run length of 337 s. The resulting motor-task data were time-trigger averaged separately for each wavelength on the onset of motor activation. Thus, each data point in the reported time series represents an average of 10 points in the original data. Six time series pairs (830 nm paired with each wavelength below 800 nm) were analyzed using the MBLL. Each subject was tested twice with a slightly different probe positions (~1-cm displacement). Our measure of concentration change was an average of the period from 10 to 12.4 s (30 data points) following the start of the stimulus, having first zero-corrected concentrations at time 0 s. We simultaneously measured pulse oximetry (Nelcore N-200) and respiration (Sleep-mate/Newlife Technologies, Resp-EZ) on all subjects.

Monte Carlo simulations

General approach

The rules used for photon migration as employed in any Monte Carlo program are described by Jacques and Wang (1995) and Wang et al. (1995). To summarize, the initial position and direction of the photon are defined as coming from a point source with a defined direction and entering the medium on the surface. Given the initial position and direction of the photon, the length to the first scattering event, L, is calculated from an exponential distribution. Absorption of the photon is considered by decreasing the photon weight by $\exp(-\mu_a L)$, where μ_a is the absorption coefficient and L is the length traveled by the photon (Wang et al., 1995). The photon is moved this distance through the tissue and then a scattering angle is calculated using the probability distribution given by the Henyey–Greenstein phase function (Wang et al., 1995), and a new scattering length is determined from an exponential distribution. The photon is propagated this new distance in the new direction. This process continues until the photon exits the medium or has traveled longer than 10 ns, because the probability of photon detection in tissue after such a period of time is exceedingly small. When the photon does try to leave the medium, the probability of an internal reflection is calculated using Fresnel's equation (Haskell et al., 1994; Wang et al., 1995). If a reflection occurs, the photon is reflected back into the medium and migration continues. Details about the Monte Carlo code can be found in Boas et al. (2002). We use the Monte Carlo approach here, instead of the Born approximation used in Boas et al. (2001), because Monte Carlo methods provide an accurate solution of photon migration through the head that is not biased by diffusion approximations. Previous work of this sort has examined partial volume effects (e.g., Okada et al., 1997) and spatial sensitivity patterns from diffuse optical probes (e.g., Firbank et al., 1998; Okada et al., 1997). To estimate the variability in our Monte Carlo results, we ran multiple, independent simulations each with a new random number seed.

Anatomical head segmentation and associated Monte Carlo parameters

Fig. 1 shows examples of the various Monte Carlo simulations. Each was performed on an anatomical MRI of a human head, 1 × 1 × 1 mm resolution that was semiautonomously segmented into six tissue types (air, scalp, skull, cerebral spinal fluid, gray/white matter, and activated brain tissue). To summarize the segmentation process, three anatomical scans were obtained on a Siemens Sonata 1.5T MRI scanner (T1-EPI, TR = 8 s, TE = 39 ms, $\theta = 90°$, 27 slices, thickness 5 mm, skip 0.75 mm; T2-FSE, TR = 10 s, TE = 48 ms, $\theta = 120°$, 27 slices, thickness 5 mm, skip 0.75 mm; 3D SPGR, TR = 7.25 ms, TE = 3.2 ms, $\theta = 7°$, 128 partitions, effective thickness 1.33 mm) and were then coregistered. Separate measures and thresholds were used for each tissue type (air = all, scalp = T2, skull = SPGR/T2, CSF = T2/SPGR, brain = SPGR) resulting in all voxels labeled as one of these five tissue types. To these tissue types we artificially added a tissue type for activated brain tissue (a subset of brain tissue voxels), the size and location of which differed across simulations (see below). The contour overlay in Fig. 1 indicates the photon migration spatial sensitivity profile for continuous-wave measurements produced by Monte Carlo simulation. One contour line is shown for each half order of magnitude (10 dB) change in the sensitivity of OD to changes in μ_a, and the contours end after 5 orders of magnitude (100 dB). For all our simulations, we needed to assume values for μ_s' and μ_a for each tissue type and each wavelength. Given the wide variation the μ_a and μ_s' parameters that have been reported (e.g., Bevilacqua et al., 1999; Okada et al., 1997; Torricelli et al., 2001), we chose the intermediate values found in Table 1 (where HbT is total hemoglobin and StO_2 is the tissue oxygen saturation). We approximated the wavelength dependence of μ_s' by $\mu_s'(\lambda) = \mu_s'(690) - 0.01 * (\lambda - 690)$—a linear approximation being adequate for the narrow wavelength range we are considering—where $\mu_s'(690)$ came from Farrell et al. (1992).

Probe geometry

We employed several different probe geometries, depending on the systematic error under investigation. For simulations of position, we kept the region of functional activation fixed and moved the source-detector pair in 0.5-cm increments along the surface of the head, always maintaining the 3-cm source-detector separation. Probe movements were made in both the medial–lateral direction (with extremes shown Figs. 1a and b) and the anterior–posterior direction (i.e., through plane, not shown). For simulations investigating species distribution and dual activations, only one probe location was used, namely the one where the primary activation was approximately centered below and between the source-detector pair and again the source-detector separation was maintained at 3 cm.

Simulated brain activation

Regions of brain activation were chosen to be brain-tissue-only voxels within cubical blocks located at the surface of the cortex. Thus, for simulation purposes the activation existed only in anatomically defined brain and not in CSF or overlying tissues. For the species distribution simulations, the volume of HbR change was fixed (specifically

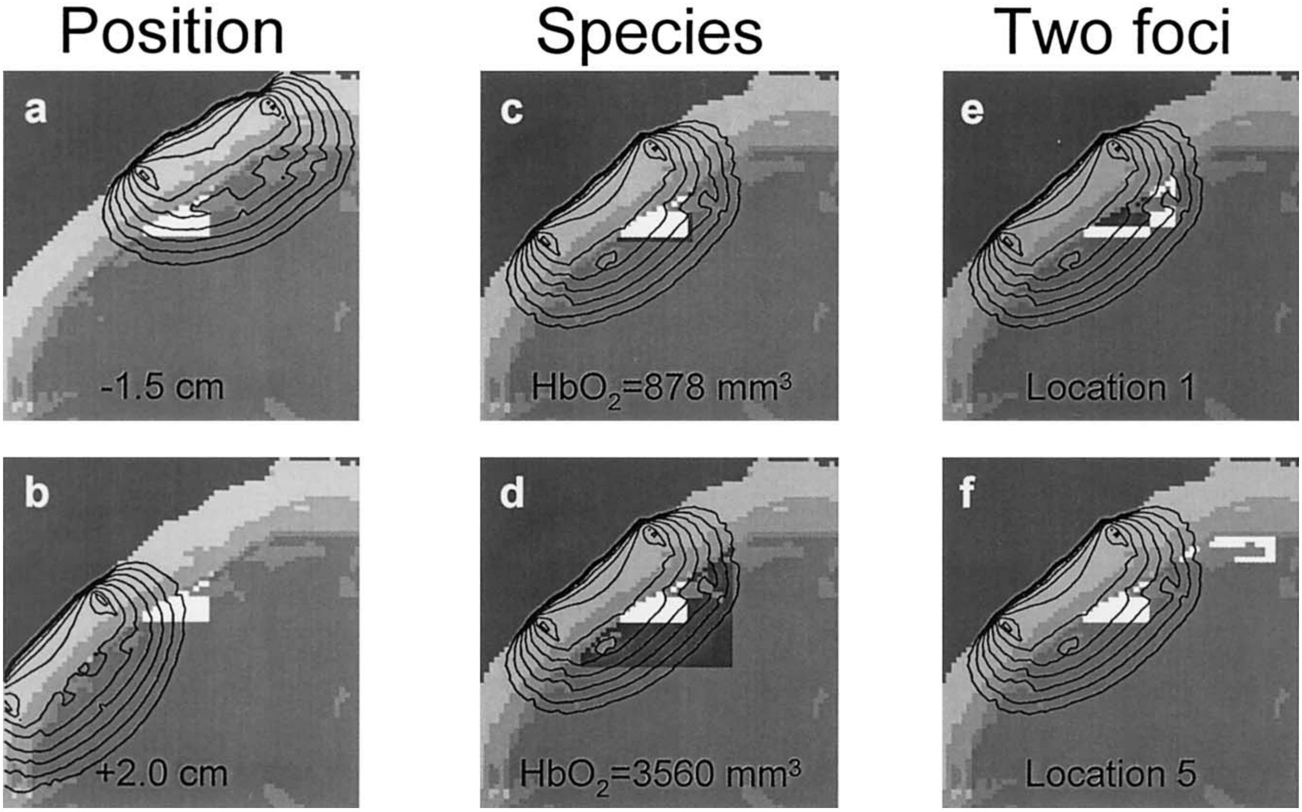

Fig. 1. Illustrations of the extreme cases for the three types of Monte Carlo simulations. (a and b) The two extremes in simulation geometry for position, shown for medial–lateral probe movement. White indicates the (fixed) region of activation, and contours indicate the source-detector probe sensitivity pattern. (c and d) The two extremes in HbO$_2$-region size for the simulations of noncoincident HbR–HbO$_2$ changes. White indicates region of HbR + HbO$_2$ change, while the darker surround indicates the extended region of HbO$_2$ change. (e and f) The two extremes in location of a secondary region of activation for the dual-activation focus simulations. Primary region of activation is fixed below and between the source and detector; the darkest region in (e) indicates an overlap between secondary and primary activations.

to that shown in Fig. 5a), encompassing a volume of 648 mm^3. The volume of HbO$_2$ change, in contrast, was increased in square shells (adding 1 mm inferior and medial to the existing activation). The resulting eight volumes were 878, 1140, 1430, 1759, 2131, 2555, 3038, and 3560 mm^3 in size. The two extremes are depicted in Figs. 1c and d. For the dual-activation conditions, the first, primary activation assumed colocalized HbR and HbO$_2$ changes, positioned at the HbR location just described. The secondary activation also assumed colocalized HbR and HbO$_2$ changes and was moved in five steps from the location of the first, 5 mm medially and 2.5 mm superiorly per step, along the surface of the brain (extremes are again shown in Figs. 1e and f). The volume of this secondary activation was 614 mm^3 (at the point of maximum overlap or 5 mm lateral displacement), 654, 608, 728, and finally 594 mm^3 at 25 mm displacement.

Monte Carlo data analysis

Three main measures were computed from the Monte Carlo data: DPF, PPF, and cross-talk. The DPF for a given source-detector pair was calculated as the actual mean pathlength traveled by all photons leaving the source that reached the detector, divided by the source-detector separation (30 mm). The PPF was calculated as the mean pathlength traveled through a given region of activation (i.e., regions of concentration change) of these same photons, also divided by the source-detector separation. Cross-talk

Table 1
Monte Carlo simulation parameters (μ_a/μ_s', both in cm^{-1})

Region/parameter	690 nm	760 nm	780 nm	830 nm	[HbT] (μM)	StO$_2$ (%)
Scalp	0.159/8.0	0.177/7.3	0.164/7.1	0.191/6.6	75	75
Skull	0.101/10.0	0.125/9.3	0.115/9.1	0.136/8.6	75	75
Cerebrospinal fluid	0.004/0.1	0.021/0.1	0.017/0.1	0.026/0.1	0	0
Brain (gray + white)	0.178/12.5	0.195/11.8	0.170/11.6	0.186/11.1	75	65

between species was determined by calculating C from Eqs. (4) and (5).

Results

Wavelength selection

NIRS in vivo measurements

Fig. 2 shows the block-averaged results from an example subject during the motor task, selecting the NIRS detector showing the maximum signal modulation from baseline during motor activity. Fig. 2a shows the measured DPF values at each of eight wavelengths for an example subject. The absolute values of these measures are above reported values (Duncan et al., 1996), resulting from small (1–2 mm), random errors in the source-detector separation measurement. The spectral dependence of the DPF values, however, agree to within ~20% with those found in the literature, and it is the spectral dependence that is relevant to the present results. Fig. 2a also shows an "altered" version of the DPFs wherein the value for 830 was reduced by 10% and the values at the other three wavelengths considered were increased by 10% (for a 20% total difference, per literature variation). The altered DPFs provide a rough indication about the sensitivity of our computed concentrations to typical variations in the pathlength factor. In Figs. 2b–d, the red and orange lines represent the calculated concentration change in HbO_2 using the measured and altered DPFs, respectively. Notice that $\Delta[HbO_2]$ differs when modulating the DPF, but the relative magnitude of this change is small. Similarly, the dark and light blue lines show the calculated $\Delta[HbR]$ using the measured versus altered DPF, respectively. Notable with the 780- and 830-nm wavelength pair, DPF variation induces a nearly 50% magnitude change in the computed $\Delta[HbR]$. This change is significant for $t = 12$ through 23 s (Student's t test, $P < 0.05$).

In Fig. 3, we compare the results from three subjects, with a and b representing the two measurements from each subject. Concentration changes were computed by subtracting $t = 0$ from an average of data from 10 to 12.4 s following stimulus onset (a total of 30 data points). Each bar in Fig. 3 represents the effect of altering the DPFs for the three wavelength pairs for each measurement. In particular, a bar represents the concentration change calculated using the measured DPFs subtracted from the concentration change calculated using the altered DPFs. Error bars represent the standard deviation of the 30 time points. It is clear that DPF modulation strongly affects the calculated changes in both [HbR] and $[HbO_2]$. Importantly, in every case the largest modulation and the most variability occurs when pairing 830 nm with a wavelength higher than 770 nm, and this difference is significant from the other wavelength pairs in all cases (Student's t tests, $P < 0.02$). We note that significant task-related heart rate increases (~15 bpm) were recorded in two of the three subjects during the experiment. However, the temporal profile of these changes did not match that of the functional activation (being both delayed 3–6 s from the activation rise and of a different shape), and the optical signals and magnitudes differed across source-detector pairs. We therefore feel justified in inferring that the reported changes include a significant contribution from brain-related activation.

In the experiment just described, we found more noise (random and systematic) in our HbR and HbO_2 measures when using 780 nm paired with 830 nm compared to other wavelength pairs. To examine this further, we plotted the absorption spectra for total hemoglobin ($HbT = HbR + HbO_2$) as a function of tissue oxygen saturation (StO_2, Fig. 4a) and the resulting theoretical sensitivity of saturation measurements (as measured by $\Delta\mu_a$) to wavelength choice (Fig. 4b). The latter curves are created by writing $StO_2 = HbO_2/(HbR + HbO_2)$ in terms of the components in Eq. (2) and solving for μ_{a1}/μ_{a2} as a function of StO_2. The steepness of the curves in Fig. 4b indicates the sensitivity of the calculated oxygen saturation to a measured change in the ratio of $\Delta\mu_a$. Thus, a steep curve indicates that a small error in the estimated μ_a ratio will produce a large error in measured calculated oxygen saturation. Notice that the 780-nm curve is the steepest of the wavelengths we used experimentally, suggesting that the 780- to 830-nm wavelength pair will be highly sensitive to all noise—systematic or random—in the μ_a estimates. This is in agreement with a recent publication indicating similar results in the presence of random noise (Yamashita et al., 2001). Fig. 4c further shows that the sensitivity to cross-talk (governed by parameters A, B, and D in Eq. (6)) grows quickly with wavelengths greater than approximately 770 nm when paired with 830 nm.

Theory and Monte Carlo simulations

We further examined the wavelength effect via Monte Carlo simulation. Fig. 5a shows the results of an example simulation as applied to our segmented head model using optical properties for the tissue layers consistent with 830-nm light. Each contour represents a half order of magnitude change in the measured OD sensitivity to changes in μ_a, with the outermost contour representing a loss of five orders of magnitude. Given our optical instrument sensitivity, we believe that we are sensitive to approximately the outermost 1 cm of brain tissue. In Fig. 5b we display a scaled version of the measured DPF along with the computed PPF for the white activation region shown in Fig. 5a, as determined at 691, 752, 780, and 830 nm. It is clear that the relative magnitudes of the PPF can differ from those of the DPFs by 20% or more, depending on wavelength pair. The behavior at 750 nm results from the fact that the PPF for deep (1–2 cm down) focal activation is highly attenuated by the absorption coefficient (which shows a small peak around 750 nm), whereas the DPF is equally sensitive to changes in absorption and scattering.

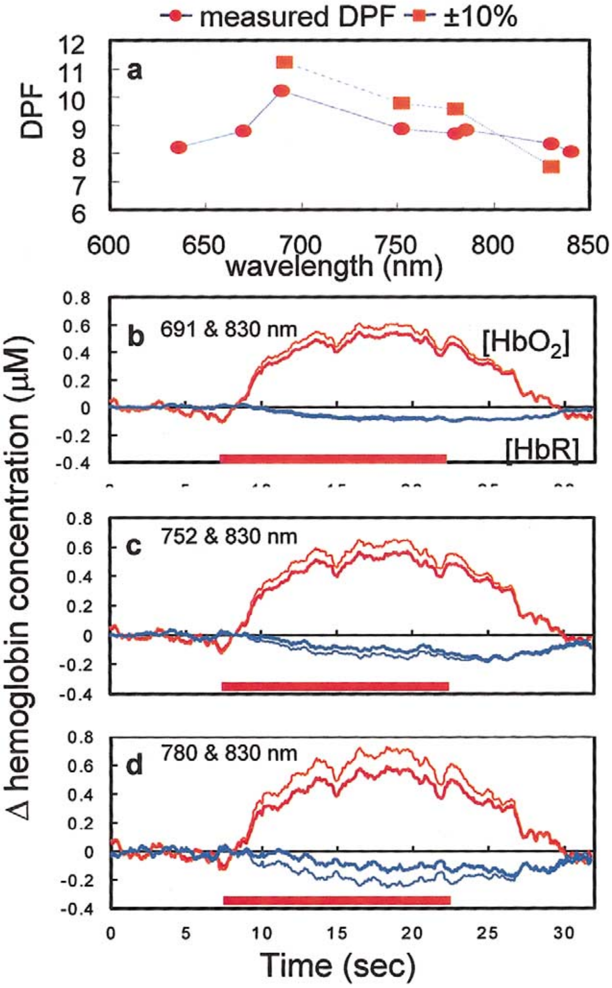

2

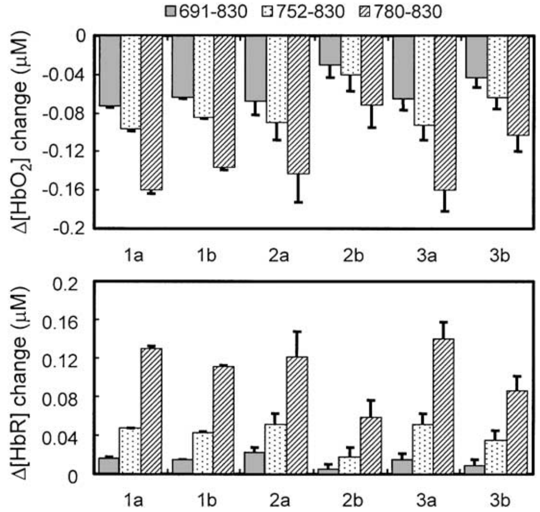

Fig. 3. Change in observed modulation depth of [HbO$_2$] (top) and [HbR] (bottom)—measured at the peak of the activation period (10 to 12.4 s from the start of the stimulus)—when subtracting the modulation depth derived from measured DPF values from the modulation depth derived from the altered DPF. The bars thus indicate how much of an effect DPF has on modulation depth, and the error bars are the standard deviation across 30 time points (2.4 s). Numbers 1–3 indicate subjects, and letters a and b indicate the two measurements for each subject; the 780–830 bar for a given subject is always significantly different from the other two bars (Student's test, $P < 0.02$).

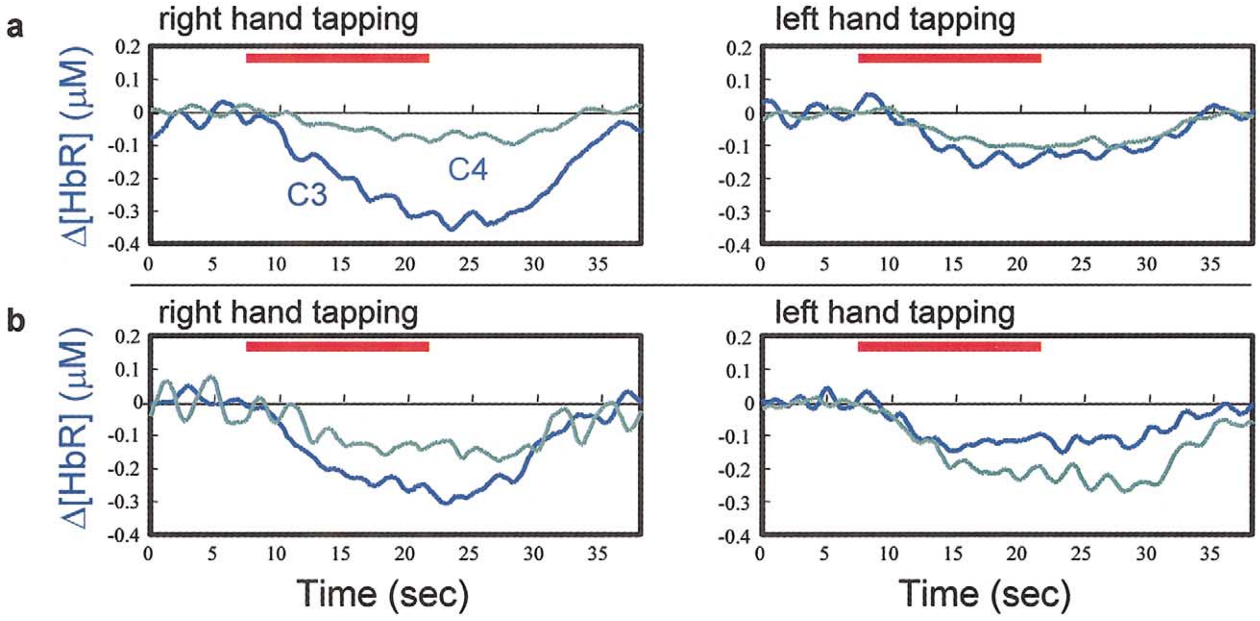

6

Fig. 2. (a) Measured DPF at eight wavelengths for subject 1, along with altered DPFs at the four wavelengths considered in this paper (830 nm reduced by 10%; other wavelengths increased by 10%). (b–d) Δ[HbR] and Δ[HbO$_2$] for the same subject performing the motor task, computed using different, simultaneously collected wavelength pairs. Pairs of curves were calculated from the measured and altered DPFs shown in (a). Standard errors at each point are on the order of 0.03 μM.

Fig. 6. Hemisphere comparison of two probe positions during the motor task, using 691 and 830 nm. (a) Time courses for Δ[HbR] from EEG 10–20 location C3 (left primary sensorimotor cortex) and C4 (right primary sensorimotor cortex) during the motor task. (b) Time courses for Δ[HbR] from location C3 and C4 during the motor task in the same subject, after repositioning the optical probe by ~1 cm.

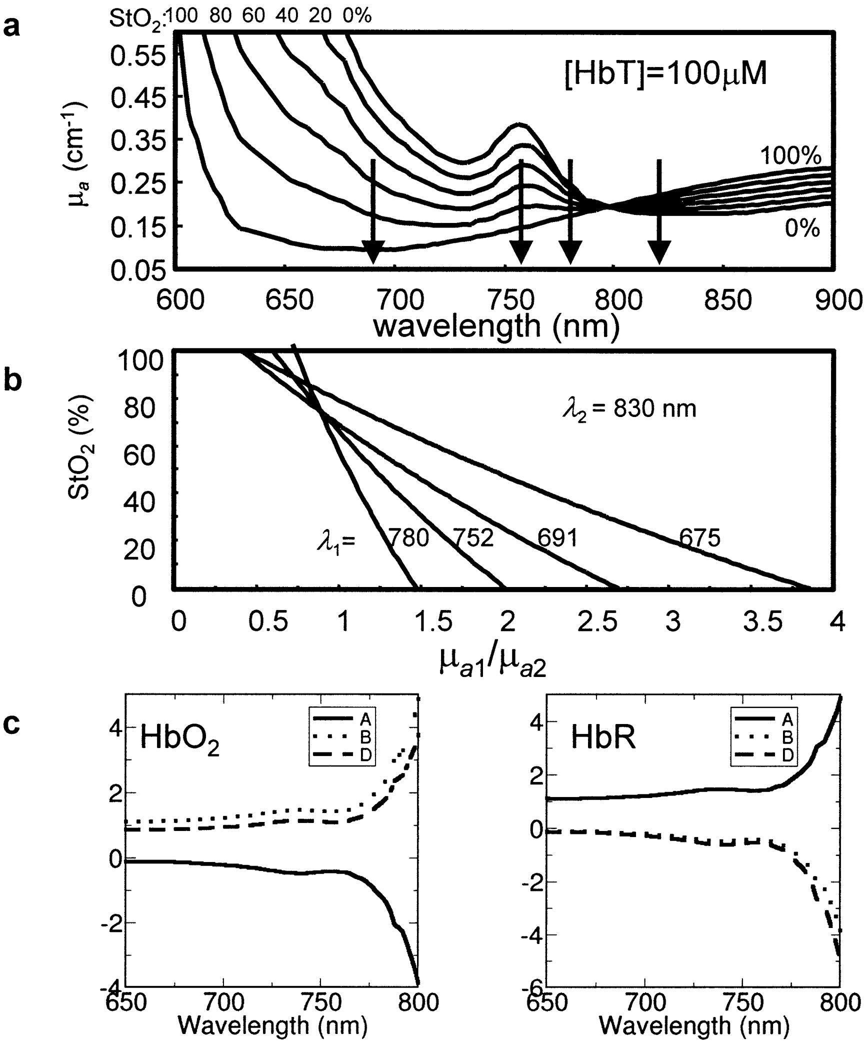

Fig. 4. (a) Overall hemoglobin absorption coefficient (HbR + HbO_2) as a function of wavelength and oxygen saturation. Arrows indicate wavelengths considered in the present study. (b) Hemoglobin saturation plotted against the ratio $\Delta\mu_a(\lambda)/\Delta\mu_a(830)$, for several wavelengths, λ. Steeper curves indicate a greater change in calculated saturation as a function of error in $\Delta\mu_a$. (c) Parameters A, B, and D from Eq. (6) are plotted for both HbO_2 and HbR with $\lambda_2 = 830$ nm. The curves are relatively flat up to approximately 770 nm, at which point the potential for cross-talk grows quickly.

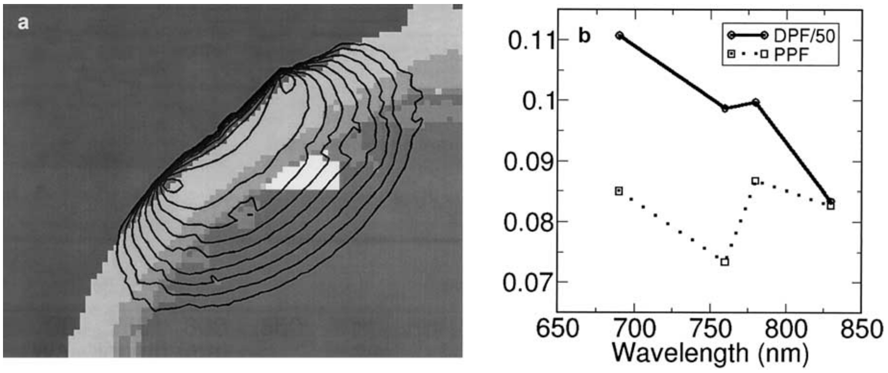

Fig. 5. (a) Monte Carlo sensitivity profile at 830 nm overlain on the segmented brain, with “activated” voxels appearing in white. (b) A comparison of the DPFs and PPFs for four different colors propagating through the geometry shown in (a). Uncertainty in the PPF owing to noise in the Monte Carlo simulation is 5% (or ~0.005 units).

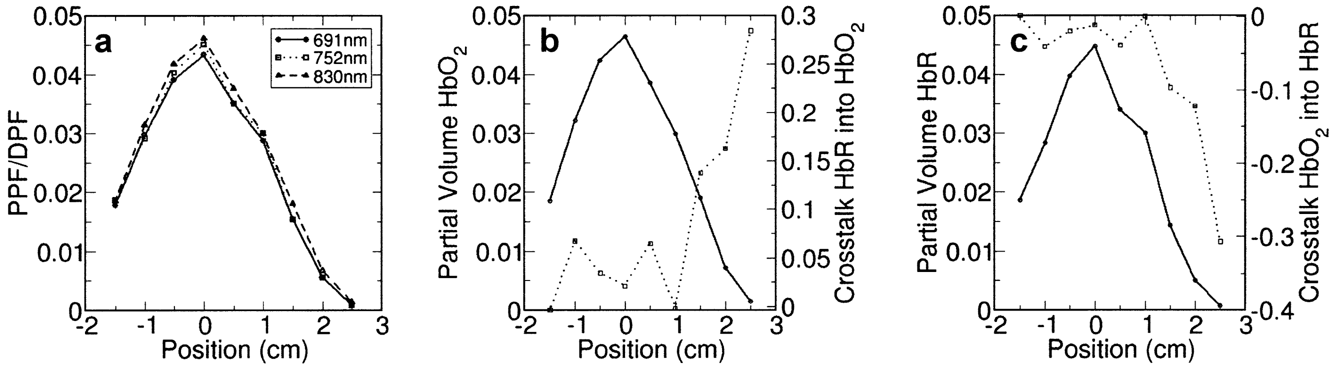

Fig. 7. Plots for the Monte Carlo simulations of medial–lateral position displacement. (a) The ratio of computed PPF to computed DPF as a function of the source-detector pair location relative to the activated region. Measurements indicate distance from the center of the activated region, along the source-detector line. Errors in the points at position 0, measured across five independent sets of Monte Carlo runs, were less than 1% of the PPF/DPF value. (b) Computed partial volume of HbO_2 (solid line, left *y*-axis; *P* in Eq. (6)) and cross-talk into HbO_2 (dotted line, right *y*-axis; *C*/*P* in Eq. (6)) for each medial–lateral source-detector position. Partial volume errors at position 0 averaged under 2%, and cross-talk errors at position 0 averaged 15% of the plotted value. (c) Computed partial volume of HbR (solid line, left *y*-axis; *P*) and cross-talk into HbR (dotted line, right *y*-axis; *C*/*P*) for each medial–lateral source-detector position. Partial volume and cross-talk errors for HbR resulting from the Monte Carlo simulations were comparable to those for HbO_2.

Location of focal change

In Fig. 6, we consider experimentally the consequences of repositioning the optical probe. Fig. 6a plots the response to our motor task when recording bilaterally (over regions C3 and C4, using just 691 and 830 nm). In this case, recordings were made from 10 positions in each hemisphere and the motor task was performed first with the right hand and then with the left. The position with the largest response from each hemisphere is plotted. Notice that the change in [HbR] is largest over the right hemisphere (C3) regardless of which hand was moving. Fig. 6b plots data from an identical experimental run on the same subject, but with the optical probe ~1 cm displaced from the position in Fig. 6a. In this case, the side contralateral to the moving hand shows the largest change in [HbR], which is more in line with previous findings (e.g., Rao et al., 1993). (Results for HbO_2 were similar, but with smaller wavelength-related differences, as would be expected given the larger amplitude of HbO_2 modulations; data not shown.)

Given this experimental evidence of substantial position dependence when comparing across NIRS probes, suggested by prior theoretical arguments and empirical data (Boas et al., 2001), we sought to quantify such effects. To do so, we used Monte Carlo simulations to investigate the cross-talk between oxy- and deoxyhemoglobin in a region of activation as a function of the location of the recording source-detector pair. To start, nine simulations were performed, each employing one source location (three colors of light; we disregard 780–830 nm as a poor wavelength pair, as indicated by Fig. 3) and one detector location. Simulations were rerun each time the source-detector probe was moved 0.5 cm along the scalp in the medial–lateral direction (i.e., parallel to the source-detector line) over the fixed region of activation (cf. Figs. 1a and b). Fig. 7a shows the ratio of the calculated DPF to the calculated PPF for each of these nine positions at each of the three experimentally used wavelengths. Notice that this ratio is much closer to zero than to one, indicating that the PPF through the focal region is small relative to the DPF. As would be expected, the largest PPF occurs when there is minimal offset between the activation focus and the center of the source-detector pair and falls off rapidly with displacement. The fall-off suggests that a "miss" of slightly more than 1 cm would result in a 50% drop in sensitivity to the focal concentration change. The standard deviation in the PPF/DPF ratio across five independent Monte Carlo runs at position 0 was 0.6, 0.7, 0.3, and 0.9% of that ratio for 691, 760, 780, and 830 nm, respectively (that is, error bars are smaller than the size of the data point).

Figs. 7b and c plot the partial volumes (*P* in Eq. (6)) and cross-talk (*C* in Eq. (6), plotted as a proportion of *P*, i.e., *C*/*P*) obtained from the Monte Carlo simulations for HbO_2 (Fig. 7b) and HbR (Fig. 7c) as calculated from both the 752- to 830-nm wavelength pair (results were essentially identical for the 691- to 830-nm pair). The partial volumes (measured via the left-hand *y*-axis) simply follow the PPF/DPF ratio, peaking at 0 cm offset. (The standard deviation in the partial volume of HbR and HbO_2, again across five Monte Carlo runs, at position 0 ranged from 0.7% to 1.7% of the partial volume.) Examining the cross-talk curves (dotted lines, right-hand *y*-axis), the cross-talk into both species is essentially flat and comprises less than 5% of the partial volume effect, up to a lateral displacement of ~1 cm. To elaborate, recall that the parameter *C* represents the proportion of the other species cross-talking into the species of interest. (If $C = 0.1$ then, for example, 10% of the real $\Delta[HbO_2]$ would be added to the measured Δ[HbR] and vice versa. Notice that this could be a large relative error in, e.g., Δ[HbR] if the real $\Delta[HbO_2]$ is much greater than the real Δ[HbR].) Instead of plotting *C* directly, we more generally plot *C*/*P* to show how large this cross-talk effect is *relative*

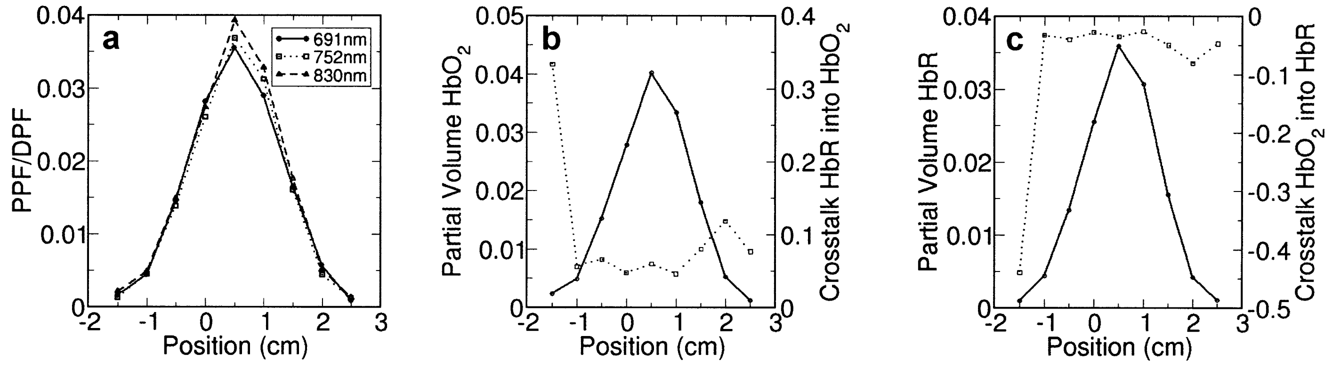

Fig. 8. Plots for the Monte Carlo simulations of anterior–posterior position displacement. (a) The ratio of computed PPF to computed DPF as a function of the source-detector pair location relative to the activated region. Measurements indicate distance from the center of the activated region, along the source-detector line. (b) Computed partial volume of HbO_2 (solid line, left y-axis; P in Eq. (6)) and cross-talk into HbO_2 (dotted line, right y-axis; C/P in Eq. (6)) for each anterior–posterior source-detector position. (c) Computed partial volume of HbR, P, and cross-talk into HbR, C, for each anterior–posterior source-detector position; same legend as for (b). Errors are comparable to those reported in Fig. 7.

to the partial volume effect. We do this because noninvasive concentration measurements will typically be strongly affected (attenuated) by the partial volume effect, and we want to determine what proportional error in the measured concentration can be attributed specifically to cross-talk. In an experimental situation where the center of the source-detector line lies within 1 cm of the measured activation, this proportional error owing to cross-talk should be less than ~5%. However, the magnitude of the cross-talk still depends on the relative magnitudes of the real Δ[HbR] and $\Delta[HbO_2]$ and thus 5% of the $\Delta[HbO_2]$ may be a large fraction of the Δ[HbR]. That is, in Eq. (5) C could be a small proportion of P but still contribute substantial error to the measured species of interest, depending on the real concentration changes in the other species. The remaining cross-talk (C/P) curves can be interpreted in exactly this manner. (The standard deviation in cross-talk across Monte Carlo runs at position 0 averaged 15% of the plotted cross-talk value.)

Fig. 8 shows the same information as Fig. 7, but for anterior–posterior movement of the source-detector pair (again with three colors). That is, the probe remained centered medial–laterally over the activation, but was moved “through” the plane shown in Figs. 1a and b. Results are quite similar except that the raw signal and partial volumes fall off somewhat more rapidly in this transverse direction (to 50% of maximum in slightly less than 1 cm). The cross-talk remains similar (~5% for small offsets).

Hemoglobin species distribution

We next used Monte Carlo simulations to examine the possibility of a spatial distribution mismatch between HbR and HbO_2—namely, that changes in HbR are more localized than changes in HbO_2. Fig. 9a plots the ratio of calculated PPF/DPF as the spatial extent of the HbO_2 change is increased beyond the (static) boundary of the HbR change (in 1-mm rectangular shells). As the HbO_2 change becomes larger, the ratio should approach 1, because the HbO_2 change is approaching the DPF assumption of a global

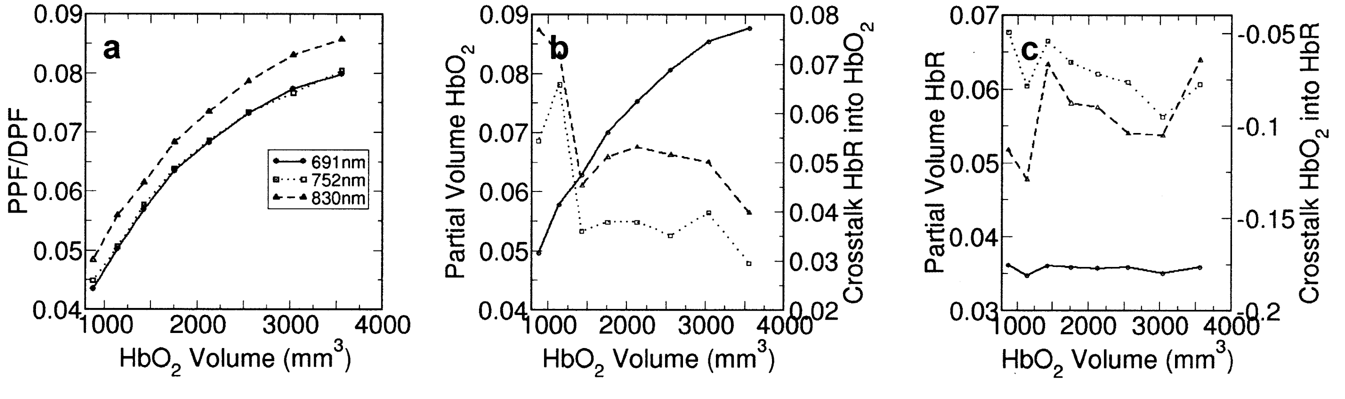

Fig. 9. Plots for the Monte Carlo simulations of hemoglobin species volume. (a) The ratio of computed PPF to computed DPF as a function of the size of the region of HbO_2 concentration change. (b) Computed partial volume of HbO_2 (solid line, left y-axis; P in Eq. (6)) and cross-talk into HbO_2 (dotted lines (691 and 752 nm), right y-axis; C/P in Eq. (6)) for different sized regions of HbO_2 concentration change. (c) Computed partial volume of HbR (solid line, left y-axis; P) and cross-talk into HbR (dotted lines (691 and 752 nm), right y-axis; C/P) for different sized regions of HbO_2 concentration change.

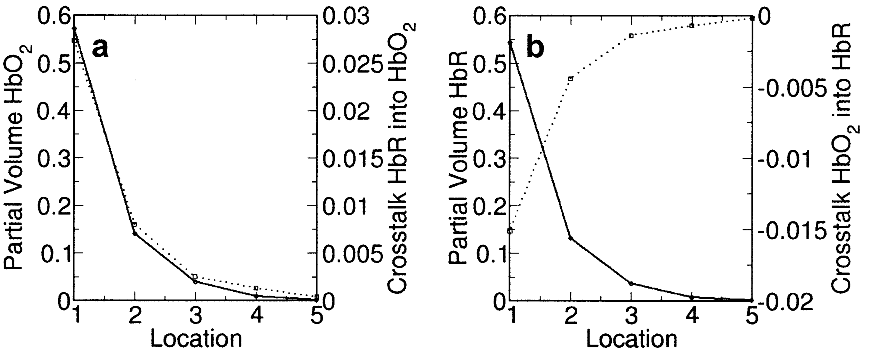

Fig. 10. Plots for the Monte Carlo simulations of a secondary activation focus. (a) Computed partial volume of HbO_2 (solid line, left y-axis; P in Eq. (6)) and cross-talk into HbO_2 (dotted line, right y-axis; C/P in Eq. (6)) for different secondary activation locations. (b) Computed partial volume of HbR (solid line, left y-axis; P) and cross-talk into HbR (dotted line, right y-axis; C/P) for different secondary activation locations. Locations 1–5 represent movements of the secondary region 5 mm medial and 2.5 mm superior from the previous region, starting from the primary activation's location.

change. While the HbO_2 activation is quite large at the farthest extreme we considered (HbO_2 volume 3560 mm^3), the ratio is nevertheless far from a ratio of 1, indicating that the assumption of global activation is still strongly violated because of the overlying scalp and skull.

Figs. 9b and c again plot the computed partial volume (P) and cross-talk (plotted as C/P) for HbO_2 (Fig. 9b) and HbR (Fig. 9c). The partial volume for HbO_2 increases as the HbO_2 activation region grows, whereas the partial volume for HbR is essentially flat. Departures from flat in the solid line in Fig. 9c demonstrate the small amount of noise generated by random number seeds in our simulations. The magnitudes of the cross-talk are considerably larger in this case than for location. The rough downward trend for cross-talk into HbO_2 arises because an essentially flat cross-talk is being divided by the increasing partial volume. It is apparent that wavelength choice more strongly modulates cross-talk here, by 25%–50% into HbO_2 and by 200%–300% into HbR. Interestingly, no single wavelength has the least cross-talk in both species.

Multiple activation regions

Finally, we considered the possibility that a second region of activation could be within the field of view of the NIRS probe during a given recording. The partial volume for the activation region centered between the source and detector and the within-region cross-talk is precisely the same as in Figs. 7–9. In Fig. 10, therefore, we simply plot the computed partial volume and cross-talk for HbO_2 and HbR (Figs. 10a and b, respectively) for the secondary activation, divided by the partial volume for HbO_2 and HbR for the primary, centered activation (that is P_β/P_α, where β represents the secondary activation and α denotes the primary activation centered below and between the source-detector pair). Thus, at the closest secondary position, the partial volume of the secondary region is greater than 50% of the partial volume of the primary activation. The associated species' sensitivity to cross-talk resulting from the second activation was also normalized to the partial volume of the primary activation or C_β/P_α. Thus, the cross-talk into HbO_2 induced by the second activation focus is approximately 3% of the expected HbO_2 concentration change when it is within ~5 mm of the main focus and drops to below 1% beyond the second position (11 mm from the primary activation). The cross-talk into HbR induced by the second activation is just over 1% of the expected HbR concentration change at the first position and quickly falls toward zero. This occurs for 752 nm as well (not shown).

Discussion

Reliable quantitation of HbR and HbO_2 concentrations using the standard approach to analyzing NIRS data is prone to a variety of systematic errors when recordings involve focal chromophore changes. For functional brain recordings, central among these errors is cross-talk between calculated HbR and HbO_2 concentrations consequent to the focal nature of the chromophore changes. In particular, if a change is focal, the relevant parameter for calculating the actual concentration change is the partial pathlength—the distance the light travels through the activated region and not the total distance the light travels from source to detector. An optical measurement will be prone to cross-talk whenever assumptions about the PPFs differ from the actual PPFs. For each of the four systematic errors we have described, however, there are at least partial solutions that help to minimize such cross-talk.

Wavelength selection

One partial solution is the choice of measurement wavelengths and recording position. Referring back to Fig. 4, it is clear that the 780- to 830-nm wavelength pair will be a less optimal choice for oxygen saturation related measurements, because a relatively small error in the measured absorption coefficient can produce a large error in the calculated saturation. This conclusion is supported by the experimental data in Fig. 3. Avoiding this wavelength pair can therefore help minimize differential sensitivity in a focal-change situation. Note that this conclusion holds even though wavelengths in this range will have substantially overlapping spatial sensitivities to the underlying tissue. Given a measurement with an infinite signal-to-noise ratio, cross-talk would indeed be minimized by choosing wavelengths with overlapping spatial sensitivities. However, the present findings indicate that the sensitivity to measurement error in this wavelength range (cf. Fig. 4) is large enough to nullify any cross-talk reduction obtained by having overlapping spatial sensitivities.

Importantly, employing more than two wavelengths—including full-spectrum approaches—will not avoid the problem. Any concentration calculation that includes data from 830 nm and a wavelength in the range of roughly 770–800 nm will provide noisy information about the actual concentration change, as shown previously (Yamashita et al., 2001). Although we have not investigated this systematically, Fig. 4c suggests that any pair of wavelengths between ~770 and 850 nm would result in similar noise issues, consequent to the small absorption spectra differences in this range. Any such noisy information will effectively be averaged together with less-noisy data from other wavelengths, reducing the validity of the concentration calculations compared to simply excluding data from any wavelengths in the 770- to 800-nm range.

Location of focal change

A more general solution to the NIRS cross-talk problem is to replace the standard DPFs with PPFs—that is, to account for the partial pathlength through the activated region. However, the location and extent of activation are typically unknown (and, in fact, often comprise a parameter of interest to the study). General statements can be made, however, even for the complicated internal tissue structure of the head. To start, it appears reasonable to assume that the activation region is indeed located below and between the source-detector pair. Experimental and theoretical results suggest that signal levels drop substantially when "off target" in either the longitudinal or the transverse directions by more than 1 cm. At the same time, species-related cross-talk was relatively stable out to 1.5–2 cm off center. Thus, when the activation is sufficiently off center for cross-talk to rise above a few percent, the signals will typically be weak. The existence of cross-talk from HbO_2 into HbR on the order of a few percent, however, can still be substantial depending on the observed magnitude HbO_2 change—a large change in HbO_2 coincident with a small change in HbR could induce 100% (or more) relative error in HbR. This consequence of course depends on the changes recorded in the particular experimental results and paradigm in question. It does appear that the relative magnitude of this cross-talk is stable (for these wavelengths) when the probe is within a ~1-cm radius of the optimal source-detector sampling region. Hence, an experimental procedure of finding the optical probe position that maximizes signal modulation should help minimize the effects of location-related cross-talk. The magnitude of our errors are in substantial agreement with the focal-activation findings recently published by Uludag et al. (2002) which specifically consider a 760- to 830-nm wavelength pairing. (Our error estimates tend to be slightly larger as a result of assuming a somewhat deeper region of focal concentration change.)

Minimizing location-related cross-talk, however, does not imply elimination of undesirable cross-talk effects. This is particularly important with regard to comparing across detectors in a NIRS experiment. Often it is desirable to demonstrate differential hemispheric lateralization for a task (e.g., when studying language tasks, visual hemi field tasks, and motor function with hand alternation). As was shown in Fig. 6, however, comparison across NIRS probes (in this case, across two hemispheres) should be undertaken with caution. The results in Fig. 6a, obtained by selecting the largest response of 10 positions in that hemisphere, obviously contradict those from Fig. 6b, which were obtained in the same way. In general, therefore, comparing amplitudes across NIRS probes is not a valid comparison. The only way to compare across spatial regions with reasonable confidence is to employ diffuse optical imaging wherein all optical measurements are evaluated for self-consistency.

Species distribution and multiple foci

We have also argued that two additional issues have the potential to affect cross-talk: a lack of colocalized changes in HbO_2 and HbR concentrations and the possibility of simultaneously detecting changes from two or more activated regions via a single source-detector pair. For noncoincident concentration changes, we found that the cross-talk was again less than 10% of the partial volume effect, over the extreme range of activation sizes investigated (again excluding 780 nm). We did not, however, investigate the situation wherein overlying tissues (e.g., scalp) show an increase in HbO_2, as might be expected when heart rate and blood pressure increases during a difficult task. Given that such changes are closer to the source and detector, they could have substantial effects on calculated concentrations, as has been argued elsewhere (Firbank et al., 1998).

For our dual-activation simulations, we found that, in addition to a few percent of within-focus cross-talk, there can be cross-talk on the order of a few more percent when a second region of activation is closer than 1 cm. If the second activation is more than 1 cm away, the between-focus cross-talk is likely to remain negligible.

Conclusions

NIRS recordings are potentially sensitive to several sources of systematic error, and such errors can be substantial in the cases of dramatic differences in concentration changes (especially cross-talk into HbR when $\Delta[\mathrm{HbO_2}] \gg \Delta[\mathrm{HbR}]$). However, there are ways to minimize such errors. One way of doing so is choosing wavelengths appropriate for the preparation. In a NIRS recording setting, at least where focal changes are expected, pairing 780 nm with 830 nm is inferior for measuring oxygenation changes compared to pairing 690 or 760 nm with 830 nm. Theoretical considerations suggested that in fact all wavelengths in the 770- to 800-nm range will provide similarly poor oxygenation information. A secondary solution is to position probes as close as possible to the location of change—which is typically achieved by selecting a recording location to maximize signal contrast. Our findings indicate that these approaches can limit such errors to a small fraction ($<$10%) of the observed concentration changes. Implementing these approaches, plus an awareness of the appropriate magnitude of any remaining errors, should afford stronger interpretation of NIRS recording data than has heretofore been possible. In particular, we believe these findings can help avoid under- or overinterpretation of small measured concentration changes (especially in HbR) from future NIRS experiments.

Acknowledgments

We thank Shalini Nadgir for technical assistance during the in vivo measurements. We acknowledge support from the NINDS (F32-NS10567 and R29-NS38842), NCRR (P41-RR14075), NIMH (R01-MH62854), and the National Space Biomedical Research Institute through NASA Cooperative Agreement NCC 9-58. This research was funded in part by the US Army, under Cooperative Agreement DAMD17-99-2-9001. This publication does not necessarily reflect the position or the policy of the Government, and no official endorsement should be inferred.

References

Aldrich, C., D'Antona, D., Spencer, J., Wyatt, J., Peebles, D., Delpy, D., Reynolds, E., 1994. Fetal cerebral oxygenation measured by near-infrared spectroscopy shortly before birth and acid-base status at birth. Obstet. Gynecol. 84, 861–866.

Bevilacqua, F., Piguet, D., Marquet, P., Gross, J.D., Tromberg, B.J., Depeursinge, C., 1999. In vivo local determination of tissue optical properties: applications to human brain. Appl. Opt. 38, 4939–4950.

Boas, D.A., Culver, J., Stott, J., Dunn, A.K., 2002. Three dimensional Monte Carlo code for photon migration through complex heterogeneous media including the adult head. Opt. Express 10, 159–170.

Boas, D.A., Gaudette, T., Strangman, G., Cheng, X., Marota, J.J.A., Mandeville, J.B., 2001. The accuracy of near infrared spectroscopy and imaging during focal changes in cerebral hemodynamics. NeuroImage 13, 76–90.

Chance, B., 1991. Optical method. Annu. Rev. Biophys. Biophys. Chem. 20, 1–28.

Cope, M., van der Zee, P., Essenpreis, M., Arridge, S.R., Delpy, D.T., 1991. Data analysis methods for near infrared spectroscopy of tissue: problems in determining the relative cytochrome aa3 concentration. SPIE 1431, 251–262.

Delpy, D.T., Cope, M., van der Zee, P., Arridge, S., Wray, S., Wyatt, J., 1988. Estimation of optical pathlength through tissue from direct time of flight measurement. Phys. Med. Biol. 33, 1433–1442.

Duncan, A., Meek, J.H., Clemence, M., Elwell, C.E., Fallon, P., Tyszczuk, L., Cope, M., Delpy, D.T., 1996. Measurement of cranial optical path length as a function of age using phase resolved near infrared spectroscopy. Pediatr. Res. 39, 889–894.

Duncan, A., Meek, J.H., Clemence, M., Elwell, C.E., Tyszczuk, L., Cope, M., Delpy, D.T., 1995. Optical pathlength measurements on adult head, calf and forearm and the head of the newborn infant using phase resolved optical spectroscopy. Phys. Med. Biol. 40, 295–304.

Duong, T.Q., Kim, D.S., Ugurbil, K., Kim, S.G., 2000. Spatiotemporal dynamics of the BOLD fMRI signals: toward mapping submillimeter cortical columns using the early negative response. Magn. Reson. Med. 44, 231–242.

Elwell, C.E., Cope, M., Edwards, A.D., Wyatt, J.S., Delpy, D.T., Reynolds, E.O.R., 1994. Quantification of adult cerebral hemodynamics by near-infrared spectroscopy. J. Appl. Physiol. 77, 2753–2760.

Essenpreis, M., Elwell, C.E., Cope, M., van der Zee, P., Arridge, S.R., Delpy, D.T., 1993. Spectral dependence of temporal point spread functions in human tissues. Appl. Opt. 32, 418–425.

Fantini, S., Franceschini, M.A., Fishkin, J.B., Barbieri, B., Gratton, E., 1994. Quantitative determination of the absorption spectra of chromophores in strongly scattering media: a light-emitting-diode based technique. Appl. Opt. 33, 5204–5213.

Fantini, S., Hueber, D., Franceschini, M., Gratton, E., Rosenfeld, W., Stubblefield, P., Maulik, D., Stankovic, M., 1999. Non-invasive optical monitoring of the newborn piglet brain using continuous-wave and frequency-domain methods. Phys. Med. Biol. 44, 1543–1563.

Farrell, T.J., Patterson, M.S., Wilson, B., 1992. A diffusion theory model of spatially resolved, steady state diffuse reflectance for the noninvasive determination of tissue optical properties in vivo. Med. Phys. 19, 879–888.

Firbank, M., Okada, E., Delpy, D.T., 1998. A theoretical study of the signal contribution of regions of the adult head to near-infrared spectroscopy studies of visual evoked responses. NeuroImage 8, 69–78.

Franceschini, M., Wallace, D., Barbieri, B., Fantini, S., Mantulin, W., Pratesi, S., Donzelli, G., Gratton, E., 1997. Optical study of the skeletal muscle during exercise with a second generation frequency-domain tissue oximeter. SPIE 2979, 807–814.

Franceschini, M.A., Toronov, V., Filiaci, M.E., Gratton, E., Fantini, S., 2000. On-line optical imaging of the human brain with 160-ms temporal resolution. Opt. Expr. 6, 49–57.

Gratton, G., Maier, J.S., Fabiani, M., Mantulin, W.W., Gratton, E., 1994. Feasibility of intracranial near-infrared optical scanning. Psychophysiology 31, 211–215.

Haskell, R.C., Svaasand, L.O., Tsay, T., Feng, T., McAdams, M.S., Tromberg, B.J., 1994. Boundary conditions for the diffusion equation in radiative transfer. J. Opt. Soc. Am. A 11, 2727–2741.

Hiraoka, M., Firbank, M., Essenpreis, M., Cope, M., Arridge, S.R., van der Zee, P., Delpy, D.T., 1993. A Monte Carlo investigation of optical pathlength in inhomogeneous tissue and its application to near-infrared spectroscopy. Phys. Med. Biol. 38, 1859–1876.

Hock, C., Muller-Spahn, F., Schuh-Hofer, S., Hofmann, M., Dirnagl, U., Villringer, A., 1995. Age dependency of changes in cerebral hemoglobin oxygenation during brain activation: a near-infrared spectroscopy study. J. Cereb. Blood Flow Metab. 15, 1103–1108.

Hu, X., Le, T.H., Ugurbil, K., 1997. Evaluation of the early response in fMRI in individual subjects using short stimulus duration. Magn. Reson. Med. 37, 877–884.

Hueber, D., Franceschini, M., Ma, H., Xu, Q., Ballesteros, J., Fantini, S., Wallace, D., Ntziachristos, V., Chance, B., 2001. Non-invasive and quantitative near-infrared hemoglobin spectrometry in the piglet brain during hypoxic stress, using a frequency-domain multi-distance instrument. Phys. Med. Biol. 46, 41–62.

Jacques, S.L., Wang, L., 1995. Monte Carlo modeling of light transport in tissues, in: Welch, A.J., van Gemert, J.C. (Eds.), Optical-Thermal Response of Laser-Irradiated Tissue, Plenum, New York, pp. 73–100.

Jobsis, F.F., 1977. Noninvasive infrared monitoring of cerebral and myocardial sufficiency and circulatory parameters. Science 198, 1264–1267.

Kohl, M., Nolte, C., Heekeren, H.R., Horst, S., Scholz, U., Obrig, H., Villringer, A., 1998. Changes in cytochrome-oxidase oxidation in the occipital cortex during visual stimulation: improvement in sensitivity by the determination of the wavelength dependence of the differental pathlength factor. Proc. PIE 3194, 18–27.

Kurth, C.D., Steven, J.M., Benaron, D.A., Chance, B., 1993. Near-infrared monitoring of cerebral circulation. J. Clin. Monit. 9, 163–170.

Nioka, S., Moser, D., Lech, G., Evengelisti, M., Verde, T., Chance, B., Kuno, S., 1998. Muscle deoxygenation in aerobic and anaerobic exercise. Adv. Exp. Med. Biol. 454, 63–70.

Nollert, G., Jonas, R.A., Reichart, B., 2000. Optimizing cerebral oxygenation during cardiac surgery: a review of experimental and clinical investigations with near infrared spectrophotometry. Thorac. Cardiovasc. Surg. 48, 247–253.

Okada, E., Firbank, M., Schweiger, M., Arridge, S.R., Cope, M., Delpy, D.T., 1997. Theoretical and experimental investigation of near-infrared light propagation in a model of the adult head. Appl. Opt. 36, 21–31.

Parilla, B.V., Tamura, R.K., Cohen, L.S., Clark, E., 1997. Lack of effect of antenatal indomethacin on fetal cerebral blood flow. Am. J. Obstet. Gynecol. 176, 1166–1171.

Peebles, D.M., Edwards, A.D., Wyatt, J.S., Cope, M., Delpy, D.T., Reynolds, E.O.R., 1992. Changes in human fetal cerebral hemoglobin concentration and oxygenation during labor measured by near-infrared spectroscopy. Am. J. Obstet. Gynecol. 166, 1369–1373.

Quaresima, V., Springett, R., Cope, M., Wyatt, J.T., Delpy, D.T., Ferrari, M., Cooper, C.E., 1998. Oxidation and reduction of cytochrome oxidase in the neonatal brain observed by in vivo near-infrared spectroscopy. Biochim. Biophys. Acta 1366, 291–300.

Rao, S.M., Binder, J.R., Bandettini, P.A., Hammeke, T.A., Yetkin, F.Z., Jesmanowicz, A., Lisk, L.M., Morris, G.L., Mueller, W.M., Estkowski, L.D., et al., 1993. Functional magnetic resonance imaging of complex human movements. Neurology 43, 2311–2318.

Steinbrink, J., Wabnitz, H., Obrig, H., Villringer, A., Rinneberg, H., 2001. Determining changes in NIR absorption using a layered model of the human head. Phys. Med. Bio. 46, 879–896.

Steinmetz, H., Furst, G., Meyer, B.U., 1989. Craniocerebral topography within the international 10–20 system. Electroencephalogr. Clin. Neurophysiol. 72, 499–506.

Tamura, M., Hoshi, Y., Okada, F., 1997. Localized near-infrared spectroscopy and functional optical imaging of brain activity. Philos. Trans. R. Soc. Lond. B. Biol. Sci. 352, 737–742.

Torricelli, A., Pifferi, A., Taroni, P., Giambattistelli, E., Cubeddu, R., 2001. In vivo optical characterization of human tissues from 610 to 1010 nm by time-resolved reflectance spectroscopy. Phys. Med. Biol. 46, 2227–2237.

Uludag, K., Kohl, M., Steinbrink, J., Obrig, H., Villringer, A., 2002. Crosstalk in the Lambert-Beer calculation for near-infrared wavelengths estimated by Monte simulations. J. Biomed. Opt. 7, 51–59.

Villringer, A., Chance, B., 1997. Non-invasive optical spectroscopy and imaging of human brain function. Trends Neurosci. 20, 435–442.

Wang, L., Jacques, S.L., Zheng, L., 1995. MCML-Monte Carlo modeling of light transport in multi-layered tissues. Comput. Methods Prog. Biomed. 47, 131–146.

Yamashita, Y., Maki, A., Koizumi, H., 2001. Wavelength dependence of the precision of noninvasive optical measurement of oxy-, deoxy-, and total-hemoglobin concentration. Med. Phys. 28, 1108–1114.